Spin states in InAs/AlSb/GaSb semiconductor quantum wells

Jun Li, Wen Yang, and Kai Chang*
SKLSM, Institute of Semiconductors, Chinese Academy of Sciences, P.O. Box 912, Beijing 100083, China
(Received 29 December 2008; revised manuscript received 15 June 2009; published 9 July 2009)

We investigate theoretically the spin states in InAs/AlSb/GaSb broken-gap quantum wells by solving the Kane model and the Poisson equation self-consistently. The spin states in InAs/AlSb/GaSb quantum wells are quite different from those obtained by the single-band Rashba model due to the electron-hole hybridization. The Rashba spin splitting of the lowest conduction subband shows an oscillating behavior. The D'yakonov-Perel' spin-relaxation time shows several peaks with increasing the Fermi wave vector. By inserting an AlSb barrier between the InAs and GaSb layers, the hybridization can be greatly reduced. Consequently, the spin orientation, the spin splitting, and the D'yakonov-Perel' spin-relaxation time can be tuned significantly by changing the thickness of the AlSb barrier.

DOI: 10.1103/PhysRevB.80.035303 PACS number(s): 71.70.Ej, 72.25.Rb, 73.21.Ac, 73.21.Fg

I. INTRODUCTION

Heterostructures based on InAs, GaSb, and AlSb are one of the most promising systems for fundamental physics research and design of novel devices due to their advantages of high-electron mobility, narrow-band gap, strong spin-obit coupling, and more importantly the special broken-gap band line up at the InAs/GaSb interface.[1,2] In the past decades, the properties of InAs/GaSb broken-gap superlattices and quantum wells (QWs) were investigated both theoretically and experimentally.[3–14] These studies show that due to the overlap of InAs conduction band and GaSb valence band, the energy dispersion may exhibits an anticrossing behavior at a finite in-plane wave vector $\boldsymbol{k}_{\parallel} \neq 0$.[3–10] The tunneling between InAs and GaSb layers opens a minihybridization gap, which was observed experimentally.[11–14] In addition, the electrons in GaSb can move across InAs/GaSb interface into InAs layer, forming a two-dimensional electron gas in InAs side and a two-dimensional hole gas in GaSb side, which is promising for observing the Bose-Einstein condensation of excitons.[14–16] In practical applications, there have been many proposals for electronic and optical devices utilizing the unique characteristics of InAs/AlSb/GaSb system such as resonant tunneling structures,[17,18] infrared detectors,[19] and interband cascade laser diodes.[20] Recently, the spin-related properties of InAs/AlSb/GaSb system also attracted much interest. For instance, there have been a number of spintronic device proposals, including the Rashba spin filter,[21] the spin field effect transistor,[22] and the high-frequency optical modulator utilizing the spin precession.[23] Moreover, InAs/GaSb QW, such as HgTe/HgCdTe QW, is another possible candidate to demonstrate the intrinsic spin Hall effect[24] and quantum spin Hall phase[25] due to the inverted band structure.

In the previous works, the electron-hole hybridization in InAs/GaSb broken-gap QWs have been well studied.[9,10,26,27] It was shown that the "spin-up" and the "spin-down" states are affected differently by the hybridization.[9,10] This implies that the spin states near the hybridization gap (where strong hybridization occurs) in InAs/GaSb QWs should be quite different from those in conventional semiconductor QWs. Since the Fermi level of the undoped InAs/GaSb QW lies inside the hybridization gap,[28] the unusual spin states nearby would be very important for many electronic properties.

In this paper, we investigate theoretically the spin orientation (i.e., the expectation value of the Pauli operator $\boldsymbol{\sigma} \equiv 2\boldsymbol{S}$ for the electron spin $\boldsymbol{S}$ in an eigenstate), the zero-field spin splitting, and the D'yakonov-Perel' (DP) spin relaxation[29] in InAs/AlSb/GaSb QWs based on the Kane model. The charge-transfer-induced internal electric field is taken into account by solving the Kane model and the Poisson equation self-consistently. For InAs/AlSb/GaSb QWs, the spin orientation (or spin states) is significantly modified by the hybridization between the conduction band and valence band, which can be tuned by changing the thickness of AlSb barrier. The spin orientation can be measured indirectly from the Faraday rotation and, indeed, offers us a physical picture and can lead to some novel effects such as the persistent spin helix.[30] Using the grating technique and Faraday rotation, the persistent rotation of the spin orientation, i.e., spin helix of electron was observed in GaAs QW.[31] The Rashba spin splitting (RSS) exhibits oscillating features as a function of in-plane wave vector in InAs/AlSb/GaSb QW (Ref. 32) near the hybridization gap. The spin-relaxation time, which is obtained from the perturbation theory,[33] shows that the unusual spin splitting could lead to several peaks with increasing the Fermi wave vector. These unusual features all come from the strong electron-hole hybridization beyond the single-band model with linear Rashba spin-orbit interaction.[34] Interestingly, the hybridization is very sensitive to the thickness of the AlSb barrier, evidenced by a rapidly decreasing hybridization gap with increasing AlSb barrier thickness. Consequently, all the spin-related properties, including the spin orientation, the spin splitting, and the DP spin-relaxation time can be tuned by varying the thickness of AlSb barrier. The property of tunable spin states in InAs/AlSb/GaSb QWs might be useful in designing new spintronic devices.

This paper is organized as follows. In Sec. II, we describe the theoretical method based on a self-consistent calculation combining the Kane model and the Poisson equation. In Sec. III, we present the numerical results for the band structure, the spin orientation, the spin splitting, and DP spin-relaxation time in InAs/AlSb/GaSb QWs. In Sec. IV we give the conclusion.

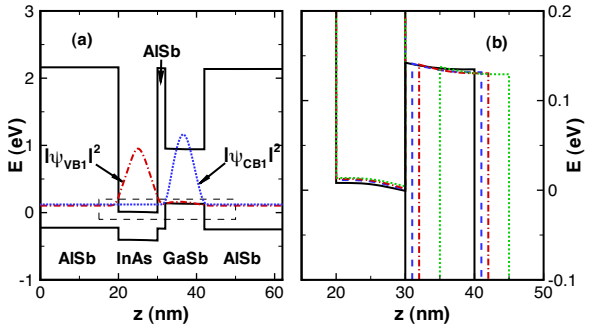

FIG. 1. (Color online) (a) Band profile and the probability density distribution of CB1(±) (blue dashdot line), VB1(±) (red dotted line) states in a 10-2-10 nm InAs/AlSb/GaSb quantum well at $k_{\|}=0$; (b) the amplification of the dashed square area in panel (a). The black solid, blue dashed, red dash dot, and green dotted lines in panel (b) denote the results of $L_{\mathrm{AlSb}}=0$, 1, 2, and 5 nm, respectively.

II. THEORY

We consider an InAs/AlSb/GaSb broken-gap QW grown along the [001] direction [see Fig. 1(a)]. We choose the axes x, y, and z to be along [100], [010], and [001], respectively. Within the envelope function approximation, the Kane model is a good starting point for systems with strong electron-hole hybridization such as InAs/AlSb/GaSb QWs. As InAs conduction band overlaps with GaSb valence band, electrons could transfer from GaSb layer into InAs layer. The charge redistribution induces an internal electric field, which can be evaluated from the Poisson equation. Generally, one needs to know the charge-density distribution to solve the Poisson equation, and the charge-density distribution is in turn determined by the electron wave function. Therefore a self-consistent procedure is needed to take the charge-transfer effect into account in this system.[35]

In Sec. II A, we discuss the Kane model and the self-consistent calculation method. To consider the spin states in broken-gap QWs, we shall give an explicit definition of spin-up and spin-down states by classifying the eigenstates of the Kane model. This is discussed in Sec. II B.

A. Hamiltonian and calculation method

Following the new envelope function theory,[36] the Kane model which describes the bulk zinc-blende semiconductors can be generalized to describe heterostructures by ordering the momentum operators with respect to material parameters. By choosing the following set of basis functions:

$$\phi_1 = \left|\frac{1}{2},\frac{1}{2}\right\rangle = |S\uparrow\rangle, \tag{1a}$$

$$\phi_2 = \left|\frac{1}{2},-\frac{1}{2}\right\rangle = |S\downarrow\rangle, \tag{1b}$$

$$\phi_3 = \left|\frac{3}{2},\frac{3}{2}\right\rangle = \frac{1}{\sqrt{2}}|(X+iY)\uparrow\rangle, \tag{1c}$$

$$\phi_4 = \left|\frac{3}{2},\frac{1}{2}\right\rangle = \frac{i}{\sqrt{6}}|(X+iY)\downarrow-2Z\uparrow\rangle, \tag{1d}$$

$$\phi_5 = \left|\frac{3}{2},-\frac{1}{2}\right\rangle = \frac{1}{\sqrt{6}}|(X-iY)\uparrow+2Z\downarrow\rangle, \tag{1e}$$

$$\phi_6 = \left|\frac{3}{2},-\frac{3}{2}\right\rangle = \frac{i}{\sqrt{2}}|X-iY\downarrow\rangle, \tag{1f}$$

$$\phi_7 = \left|\frac{1}{2},\frac{1}{2}\right\rangle = \frac{1}{\sqrt{3}}|(X+iY)\downarrow+Z\uparrow\rangle, \tag{1g}$$

$$\phi_8 = \left|\frac{1}{2},-\frac{1}{2}\right\rangle = -\frac{i}{\sqrt{3}}|(X-iY)\uparrow-Z\downarrow\rangle, \tag{1h}$$

the Kane Hamiltonian for zinc-blende crystals near the Γ point is

$$H_k = \begin{bmatrix}
A & 0 & i\sqrt{3}V^\dagger & \sqrt{2}U & iV & 0 & iU & \sqrt{2}V \\
0 & A & 0 & -V^\dagger & i\sqrt{2}U & -\sqrt{3}V & i\sqrt{2}V^\dagger & -U \\
-i\sqrt{3}V & 0 & -(P+Q) & L & M & 0 & \frac{i}{\sqrt{2}}L & -i\sqrt{2}M \\
\sqrt{2}U & -V & L^\dagger & -(P-Q) & 0 & M & i\sqrt{2}Q & i\sqrt{\frac{3}{2}}L \\
-iV^\dagger & -i\sqrt{2}U & M^\dagger & 0 & -(P-Q) & -L & -i\sqrt{\frac{3}{2}}L^\dagger & i\sqrt{2}Q \\
0 & -\sqrt{3}V^\dagger & 0 & M^\dagger & -L^\dagger & -(P+Q) & -i\sqrt{2}M^\dagger & -\frac{i}{\sqrt{2}}L^\dagger \\
-iU & -i\sqrt{2}V & -\frac{i}{\sqrt{2}}L^\dagger & -i\sqrt{2}Q & i\sqrt{\frac{3}{2}}L & i\sqrt{2}M & -P-\Delta & 0 \\
\sqrt{2}V^\dagger & -U & i\sqrt{2}M^\dagger & -i\sqrt{\frac{3}{2}}L^\dagger & -i\sqrt{2}Q & \frac{i}{\sqrt{2}}L & 0 & -P-\Delta
\end{bmatrix}, \tag{1i}$$

where

$$A = E_v + E_g + \boldsymbol{k} A_c \boldsymbol{k}, \tag{2a}$$

$$P = -E_v + \frac{\hbar^2}{2m_0}\boldsymbol{k}\gamma_1\boldsymbol{k}, \tag{2b}$$

$$Q = \frac{\hbar^2}{2m_0}(k_x\gamma_2 k_x + k_y\gamma_2 k_y - 2k_z\gamma_2 k_z), \tag{2c}$$

$$L = i\frac{\sqrt{3}\hbar^2}{m_0}\{k_-\gamma_3 k_z\}, \tag{2d}$$

$$M = -\frac{\sqrt{3}\hbar^2}{2m_0}[k_x\gamma_2 k_x - k_y\gamma_2 k_y - 2i\{k_x\gamma_3 k_y\}], \tag{2e}$$

$$U = \frac{1}{\sqrt{3}}P_0 k_z, \tag{2f}$$

$$V = \frac{1}{\sqrt{6}}P_0 k_-. \tag{2g}$$

In Eq. (2), $\boldsymbol{k}=(\boldsymbol{k}_\parallel, -i\partial/\partial_z)$, $k_\pm = k_x \pm ik_y$, and $\{k_\alpha\gamma k_\beta\} = (k_\alpha\gamma k_\beta + k_\beta\gamma k_\alpha)/2$ $(\alpha,\beta = x,y,z)$. Here the in-plane momentum as a constant of motion has been replaced by its eigenvalue $\boldsymbol{k}_\parallel$, and we have neglected the bulk inversion asymmetry (Dresselhaus effect) since it is small compared to the structure inversion asymmetry (Rashba effect). The strain effect is also neglected because the lattice mismatch between InAs and GaSb is less than 1%.

The band parameters are assumed to be a piecewise function along the growth direction,

$$\gamma(z) = \sum_i \gamma^j[\Theta(z - z_i) - \Theta(z - z_{i+1})], \tag{3}$$

where $\Theta(z)$ is the Heaviside step function, z_i is the ith interface of this system, and γ^j is the bulk band parameters of the ith layer. These band parameters, including E_g, E_v, Δ, A_c, γ_1, γ_2, and γ_3, can be derived from the Luttinger parameters and the electron effective mass.[37] They are given in Table I. The valence-band offset of two neighboring materials is $\Delta E_v^i = E_v^i - E_v^{i+1}$.

For thick enough InAs and GaSb layers, the lowest conduction subband in InAs layer overlaps with the highest valence subband in GaSb layer. Electrons could transfer from GaSb to InAs, inducing an internal electrostatic potential $V_{in}(z)$. Therefore, the total Hamiltonian becomes $H(\boldsymbol{k}_\parallel) = H_k(\boldsymbol{k}_\parallel) - eV_{in}(z)$. The subband dispersions and the corresponding eigenstates are obtained from the Schrödinger equation

$$H(\boldsymbol{k}_\parallel)|\Psi_s(\boldsymbol{k}_\parallel)\rangle = E_s(\boldsymbol{k}_\parallel)|\Psi_s(\boldsymbol{k}_\parallel)\rangle, \tag{4}$$

where s is the index of the subband and $|\Psi_s(\boldsymbol{k}_\parallel)\rangle = \exp(i\boldsymbol{k}_\parallel\cdot\boldsymbol{\rho})[\varphi_1^s(z), \varphi_2^s(z), \ldots, \varphi_8^s(z)]^T$ is the envelope function. To solve the Schrödinger equation, we expand φ_n^s by a series of plane waves,

TABLE I. The Kane parameters used in our calculation. These parameters are calculated from the Luttinger parameters obtained from Ref. 37 (see the formulism below). The value of Kane energy $E_p = 2m_0P_0^2/\hbar^2$ is taken equal to 22.5 eV for each layer material. The relation between Kane parameters and Luttinger parameters are $\gamma_1 = \gamma_1^L - \frac{E_p}{3E_g}$, $\gamma_2 = \gamma_2^L - \frac{E_p}{6E_g}$, and $\gamma_1 = \gamma_3^L - \frac{E_p}{6E_g}$. A_c is correlated with electron effective mass m^* by $A_c = \frac{\hbar^2}{2m^*} - \frac{E_p}{6m_0}(\frac{2}{E_g} + \frac{1}{E_g+\Delta})$.

	InAs	GaSb	AlSb
E_g (eV)	0.417	0.812	2.386
E_v (eV)	−0.417	0.143	−0.237
Δ (eV)	0.39	0.76	0.676
A_c (eV nm^2)	−0.26	0.09	−0.06
γ_1	2.01	4.16	2.04
γ_2	−0.49	8.18	−0.38
γ_3	0.21	1.38	0.40
ε	14.55	15.69	14.4

$$\varphi_n^s(z) = \frac{1}{\sqrt{L}}\sum_{m=-N}^{N} c_{nm}^s \exp(ik_m z), \tag{5}$$

where $k_m = 2m\pi/L$ and L is the total length of the structure (in this work, $L = 2L_{\mathrm{AlSb}}^{side} + L_{\mathrm{InAs}} + L_{\mathrm{AlSb}}^{middle} + L_{\mathrm{GaSb}}$, and $L_{\mathrm{AlSb}}^{side} = 2L_{\mathrm{InAs}}$). By choosing a moderate N, one can also avoid the spurious solutions that may occur in the Kane model.[38] In our calculation, $N \approx 25$ is good enough to get convergent results.

The internal electrostatic potential $V_{in}(z)$ is determined by the Poisson equation

$$\frac{d}{dz}\varepsilon(z)\frac{d}{dz}V_{in}(z) = -[\rho_e(z) + \rho_h(z)], \tag{6}$$

where $\rho_e(z)$ and $\rho_h(z)$ are, respectively, the charge densities due to electrons and holes and $\varepsilon(z)$ is the static dielectric constant. $\rho_e(z)$ and $\rho_h(z)$ can be derived from the envelope functions,

$$\rho_e(z) = -\frac{e}{(2\pi)^2}\sum_s \int \sum_{n=1,2} |\varphi_n^s(z)|^2 f_F(E_s) d\boldsymbol{k}_\parallel, \tag{7}$$

$$\rho_h(z) = \frac{e}{(2\pi)^2}\sum_s \int \sum_{n=3,4,\ldots,8} |\varphi_n^s(z)|^2 [1 - f_F(E_s))] d\boldsymbol{k}_\parallel, \tag{8}$$

where $f_F(E_s)$ is the Fermi distribution function. The summations $\Sigma_{n=1,2}$ and $\Sigma_{n=3,4,\ldots,8}$ runs over the electron components ϕ_1, ϕ_2 and hole components $\phi_3, \ldots, \phi_8$, respectively. The summation Σ_s includes all the subbands which show anticrossing behavior. For simplicity, we take $T=0$ K and the axial approximation[39,40] in the self-consistent procedure. Since we want to give a clear picture about the effect of the

hybridization on the spin states, we only consider the anticrossing occurs when the lowest conduction subband meets the highest valence subband, which limits to the two cases $L_{\mathrm{InAs}} \leq 14$ nm at $L_{\mathrm{GaSb}}=10$ nm and $L_{\mathrm{GaSb}} \leq 14$ nm at $L_{\mathrm{InAs}}=10$ nm.

The Fermi level E_F is determined by the charge neutrality condition,

$$\int_0^L [\rho_e(z) + \rho_h(z)]dz = 0. \tag{9}$$

The Fermi level E_F obtained by Eqs. (7)–(9) locates closely above the minigap.[28,41] Combining Eqs. (4)–(9), we can do a self-consistent iteration that eventually yields the internal electrostatic potential $V_{in}(z)$. Once we have $V_{in}(z)$, the subband dispersions and electronic states can be obtained by solving Eq. (4).

B. Classification of the spin states

In the single-band Rashba model for the electron (i.e., ϕ_1 and ϕ_2 components only), there is a well-defined spin-quantization axis $\hat{\boldsymbol{e}}_\Sigma = \hat{\boldsymbol{e}}_{\boldsymbol{k}_\parallel} \times \hat{\boldsymbol{e}}_z$ perpendicular to both the wave-vector direction $\hat{\boldsymbol{e}}_{\boldsymbol{k}_\parallel}$ and the QW growth direction $\hat{\boldsymbol{e}}_z$. The spin orientation of any eigenstate always has a magnitude of unity and is either parallel (called spin-up eigenstates) or antiparallel (called spin-down eigenstates) to $\hat{\boldsymbol{e}}_\Sigma$.[42] For the $J=3/2$ hole system (i.e., components $\phi_3, \ldots, \phi_6$) or a hybridized electron-hole system,[43] however, such a quantization axis does not exist. As we shall show in Sec. III, for a given conduction subband, the spin orientation may change its magnitude and direction (up to 180°) with increasing $\boldsymbol{k}_\parallel$. The absence of a well-defined spin-quantization axis makes it impossible to classify the spin-up and spin-down states by their spin orientations relative to this quantization axis.

In the following, we divide the Kane Hamiltonian $H_k(\boldsymbol{k}_\parallel)$ in Eq. (1i) (note that bulk inversion asymmetry has been neglected) as the sum of a dominating part $H_{ax}(\boldsymbol{k}_\parallel)$ with axial symmetry and a small cubic part $H_{cub}(\boldsymbol{k}_\parallel)$ with cubic symmetry[44]

$$H_k(\boldsymbol{k}_\parallel) = H_{ax}(\boldsymbol{k}_\parallel) + H_{cub}(\boldsymbol{k}_\parallel). \tag{10}$$

The axial part $H_{ax}(\boldsymbol{k}_\parallel)$ obtained from Eq. (1i) by replacing γ_2 and γ_3 with $\bar{\gamma}$ in the term M and the cubic part $H_{cub}(\boldsymbol{k}_\parallel) \equiv H_k(\boldsymbol{k}_\parallel) - H_{ax}(\boldsymbol{k}_\parallel)$ is the difference between $H_k(\boldsymbol{k}_\parallel)$ and $H_{ax}(\boldsymbol{k}_\parallel)$.

The axial part $H_{ax}(\boldsymbol{k}_\parallel)$ can be transformed into a block-diagonal form by choosing a new basis set. Similar transformation has been reported in dealing with the four-band[39] and six-band models,[40] but the cubic part was neglected in these works. In this paper the transformation is extended to the eight-band model and the cubic part is also included. Let $\boldsymbol{k}_\parallel = k_\parallel(\cos\varphi, \sin\varphi)$ and the new basis set is φ dependent,

$$|S(-)\rangle = \frac{1}{\sqrt{2}}(i\phi_1 - e^{i\varphi}\phi_2), \quad |S(+)\rangle = \frac{1}{\sqrt{2}}(i\phi_1 + e^{i\varphi}\phi_2),$$

$$|HH(-)\rangle = \frac{e^{-i\varphi}}{\sqrt{2}}(\phi_3 + e^{3i\varphi}\phi_6),$$

$$|HH(+)\rangle = \frac{e^{-i\varphi}}{\sqrt{2}}(\phi_3 - e^{3i\varphi}\phi_6),$$

$$|LH(-)\rangle = \frac{1}{\sqrt{2}}(\phi_4 + e^{i\varphi}\phi_5), \quad |LH(+)\rangle = \frac{1}{\sqrt{2}}(\phi_4 - e^{i\varphi}\phi_5),$$

$$|SO(-)\rangle = \frac{i}{\sqrt{2}}(\phi_7 + e^{i\varphi}\phi_8), \quad |SO(+)\rangle = \frac{i}{\sqrt{2}}(\phi_7 - e^{i\varphi}\phi_8). \tag{11}$$

Under this basis, $H_{ax}(\boldsymbol{k}_\parallel) \rightarrow \mathcal{H}_{ax}(k_\parallel)$ is block diagonalized and $H_{cub}(\boldsymbol{k}_\parallel) \rightarrow \mathcal{H}_{cub}(\boldsymbol{k}_\parallel)$ has a simple dependence on the azimuth φ,

$$\mathcal{H}_{ax}(k_\parallel) = \begin{pmatrix} \mathcal{H}_-(k_\parallel) & 0 \\ 0 & \mathcal{H}_+(k_\parallel) \end{pmatrix}, \tag{12}$$

$$\mathcal{H}_{cub}(\boldsymbol{k}_\parallel) = \begin{pmatrix} \mathcal{A}(k_\parallel)\cos 4\varphi & -i\mathcal{A}(k_\parallel)\sin 4\varphi \\ i\mathcal{A}(k_\parallel)\sin 4\varphi & -\mathcal{A}(k_\parallel)\cos 4\varphi \end{pmatrix}, \tag{13}$$

where

$$\mathcal{H}_\pm(k_\parallel) = \begin{bmatrix} A & \sqrt{3}V' & -\sqrt{2}U' \mp V' & U' \mp \sqrt{2}V' \\ \sqrt{3}V' & -P-Q & L' \mp M' & -\dfrac{L' \pm 2M'}{\sqrt{2}} \\ \sqrt{2}U' \mp V' & -L' \mp M' & -P+Q & \dfrac{-2Q \pm \sqrt{3}L'}{\sqrt{2}} \\ -U' \mp \sqrt{2}V' & \dfrac{L' \mp 2M'}{\sqrt{2}} & \dfrac{-2Q \mp \sqrt{3}L'}{\sqrt{2}} & -P-\Delta \end{bmatrix}, \tag{14}$$

$$\mathcal{A}(k_\parallel) = \frac{\sqrt{3}\hbar^2 k_\parallel^2}{2m_0}\Delta\bar{\gamma}\begin{bmatrix} 0 & 0 & 0 & 0 \\ 0 & 0 & 1 & \sqrt{2} \\ 0 & 1 & 0 & 0 \\ 0 & \sqrt{2} & 0 & 0 \end{bmatrix}, \tag{15}$$

and

$$L' = i\frac{\sqrt{3}\hbar^2}{2m_0}k_\parallel(\gamma_3 k_z + k_z\gamma_3), \tag{16a}$$

$$M' = -\frac{\sqrt{3}\hbar^2}{2m_0}\bar{\gamma}k_\parallel^2, \tag{16b}$$

$$U' = \frac{i}{\sqrt{3}}P_0 k_z, \tag{16c}$$

$$V' = \frac{1}{\sqrt{6}}P_0 k_\parallel, \tag{16d}$$

$$\bar{\gamma} = \frac{1}{2}(\gamma_2 + \gamma_3), \tag{16e}$$

$$\Delta\bar{\gamma} = \frac{1}{2}(\gamma_2 - \gamma_3). \tag{16f}$$

Using the new basis set, we can give an explicit classification of all the eigenstates into spin-up and spin-down states, similar to the single-band model.

In the absence of the cubic term $\mathcal{H}_{cub}(\boldsymbol{k}_\parallel)$ (so-called axial approximation), the eigenstates $|\Psi_{s,\pm}^{(ax)}(k_\parallel)\rangle$ and eigenenergies $E_{s,\pm}^{(ax)}(k_\parallel)$ (for the sth subband) of the total Hamiltonian $H(\boldsymbol{k}_\parallel) = \mathcal{H}_{ax}(k_\parallel) - eV_{in}(z)$ are determined by

$$[\mathcal{H}_\pm(k_\parallel) - eV_{in}(z)]|\Psi_{s,\pm}^{(ax)}(k_\parallel)\rangle = E_{s,\pm}^{(ax)}(k_\parallel)|\Psi_{s,\pm}^{(ax)}(k_\parallel)\rangle, \tag{17}$$

with the Rashba spin splitting in the sth subband

$$\Delta E_s^{(ax)}(k_\parallel) = E_{s,+}^{(ax)}(k_\parallel) - E_{s,-}^{(ax)}(k_\parallel). \tag{18}$$

Obviously, the eigenstates are automatically classified into two classes: the spin-down states $|\Psi_{s,-}^{(ax)}(k_\parallel)\rangle$ consisting of the components $|S(-)\rangle$, $|HH(-)\rangle$, $|LH(-)\rangle$, and $|SO(-)\rangle$ and the spin-up states $|\Psi_{s,+}^{(ax)}(k_\parallel)\rangle$ consisting of the components $|S(+)\rangle$, $|HH(+)\rangle$, $|LH(+)\rangle$, and $|SO(+)\rangle$. Then one can define the spin orientation of an arbitrary eigenstate $|\Psi_{s,\pm}^{(ax)}(k_\parallel)\rangle$ as[42,43]

$$\langle\boldsymbol{\Sigma}^{(ax)}(\boldsymbol{k}_\parallel)\rangle_{s,\pm} = \langle\Psi_{s,\pm}^{(ax)}(k_\parallel)|\boldsymbol{\Sigma}(\varphi)|\Psi_{s,\pm}^{(ax)}(k_\parallel)\rangle, \tag{19}$$

where $\boldsymbol{\Sigma}(\varphi) \equiv [\Sigma_x(\varphi), \Sigma_y(\varphi), \Sigma_z(\varphi)]$ are 8×8 matrices (see the Appendix) for the Pauli operators $\boldsymbol{\sigma} \equiv 2\boldsymbol{S}$ in the new basis [Eq. (11)].

In the presence of the cubic part $\mathcal{H}_{cub}(\boldsymbol{k}_\parallel)$, the off-block-diagonal terms $\pm i\mathcal{A}\sin 4\varphi$ will in general couple the spin-up states with spin-down states, unless $\boldsymbol{k}_\parallel$ points along a high-symmetry axis satisfying $\sin 4\varphi = 0$. As a result, the exact eigenstate $|\Psi_s(\boldsymbol{k}_\parallel)\rangle$ of the Kane Hamiltonian is in general a mixture of spin-up and spin-down states. For convenience, however, we still classify the exact eigenstates as spin-up or spin-down states according to the dominant component.

Now we discuss the electronic structure of InAs/GaSb and InAs/AlSb/GaSb QWs in the axial approximation [$\mathcal{H}_{cub}(\boldsymbol{k}_\parallel) = 0$] and the modification due to the cubic correction $\mathcal{H}_{cub}(\boldsymbol{k}_\parallel)$. In the axial approximation, the electronic structure shows three distinct features:

(1) Electron-hole anticrossing. If the InAs and GaSb layers are thick enough, the lowest conduction subband (CB1) anticrosses with the highest valence subband (VB1) at a critical in-plane wave vector $\boldsymbol{k}_a$, evidenced by the switch of the dominant component (a) from $|HH(\pm)\rangle$ to $|S(\pm)\rangle$ for the CB1 subband state $|\Psi_{\mathrm{CB1},\pm}^{(ax)}(k_\parallel)\rangle$ and (b) from $|S(\pm)\rangle$ to $|HH(\pm)\rangle$ for the VB1 subband state $|\Psi_{\mathrm{VB1},\pm}^{(ax)}(k_\parallel)\rangle$ when $\boldsymbol{k}_\parallel$ is increased across $\boldsymbol{k}_a$.

(2) The spin orientation of $|\Psi_{s,\pm}^{(ax)}(k_\parallel)\rangle$ is always along $\hat{\boldsymbol{e}}_\Sigma = \hat{\boldsymbol{e}}_{\boldsymbol{k}_\parallel} \times \hat{\boldsymbol{e}}_z$, i.e., in the QW plane and perpendicular to the in-plane wave vector $\boldsymbol{k}_\parallel$, in agreement with the prescription of the single-band Rashba model[34,42] [this can be verified using Eqs. (A8a) and (A9c) in the Appendix]. But the projection of the spin orientation varies with $\boldsymbol{k}_\parallel$ and may even change sign, which is different from the single-band Rashba model.

(3) The Rashba spin splitting of the CB1 subband exhibits an oscillating behavior [containing zero-spin splitting (spin-degeneracy) points] due to the electron-hole anticrossing.

In the presence of the cubic correction $\mathcal{H}_{cub}(\boldsymbol{k}_\parallel)$, the following additional features are introduced: (1) The band structure and spin splitting as a function of $\boldsymbol{k}_\parallel$ display a C_{4v} symmetry. (2) The spin orientation of the exact eigenstate $|\Psi_s(\boldsymbol{k}_\parallel)\rangle$ deviates from $\hat{\boldsymbol{e}}_\Sigma = \hat{\boldsymbol{e}}_{\boldsymbol{k}_\parallel} \times \hat{\boldsymbol{e}}_z$ (although it still lies in the QW plane) due to hybridization of spin-up and spin-down states. The maximum deviation arises when the azimuth angle φ of $\boldsymbol{k}_\parallel$ satisfies $\sin(4\varphi) = \pm 1$ [such that the spin mixing matrix element in Eq. (13) reaches the maximum] and at one of the spin-degeneracy points. In Sec. III, all these special properties in InAs/GaSb and InAs/AlSb/GaSb broken-gap QWs are demonstrated by our numerical results.

III. NUMERICAL RESULTS AND DISCUSSION

In Fig. 1 we show the self-consistent band profile of an InAs/AlSb/GaSb broken-gap QWs. In this QW, the concentration of electrons transferred from GaSb layer to InAs layer is found to be on the order of 1.61×10^{11} cm^{-2}. The resulting electronstatic potential $V_{in}(z)$ induces a $8\sim 14$ meV downward (upward) bending of the InAs conduction band (GaSb valence band) near the interface and causes a slight shift of the subbands [see Fig. 1(b)]. Note that we denote the upper two branches of anticrossed subbands as CB1($\pm$) and the lower two as VB1($\pm$) (see Fig. 2), which are different from the previous works.[9,10]

In Fig. 2 we plot the band structure of InAs/AlSb/GaSb QWs with different thicknesses of middle AlSb barrier (the thicknesses of InAs and GaSb layers are fixed at 10 nm). Due to electron-hole hybridization, the CB1 and VB1 subbands exhibit a strong anticrossing behavior and open a minihy-

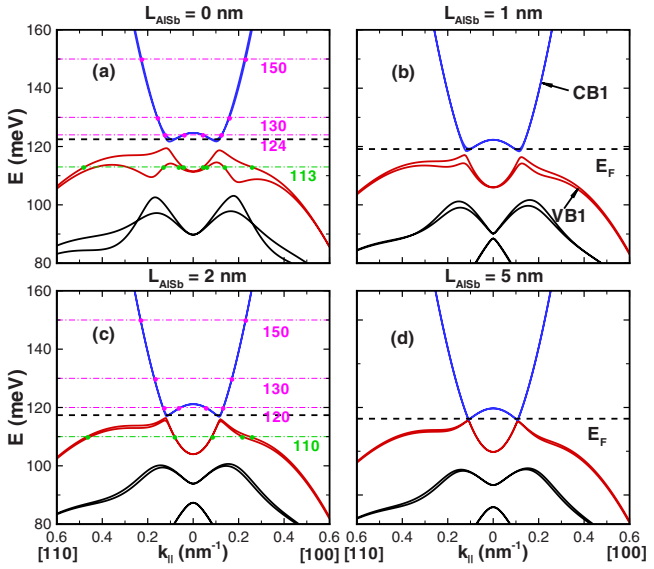

FIG. 2. (Color online) The subband dispersions of InAs/AlSb/GaSb quantum well structures with different thicknesses of AlSb layers: (a) $L_{\mathrm{AlSb}}=0$, (b) $L_{\mathrm{AlSb}}=1$ nm, (c) $L_{\mathrm{AlSb}}=2$ nm, and (d) $L_{\mathrm{AlSb}}=5$ nm. The thicknesses of InAs and GaSb layers are fixed at 10 nm. The Fermi energy denoted by the dashed lines lies at the bottom of the lowest conduction band, in agreement with previous works (Refs. 3 and 28). In panels (a) and (c), the cross points between CB1 (VB1) and the purple (green) dashed-dotted lines mark the constant energy contours drawn in Fig. 3 (Fig. 4).

bridization gap at a finite $\boldsymbol{k}_{\parallel}$, consistent with the previous works.[5–10] The resulting strongly hybridized states near the gap may have significant contributions to the spin-related properties of the broken-gap QWs since the Fermi energy (the dashed lines in Fig. 2) locates nearby.[28,41] From Figs. 2(b)–2(d), we can see that by increasing the thickness of the AlSb barrier layer, the anticrossing between CB1 and VB1 is gradually weakened and the hybridized gap is noticeably narrowed due to the tunneling between CB1 and VB1 is suppressed significantly. Meanwhile, the spin splitting of each subband is greatly reduced due to the decreasing structural inversion asymmetry in the InAs/AlSb/GaSb QW compared with the InAs/GaSb QW.

In Fig. 3(a) we show the spin orientations of the eigenstates on different constant energy contours of CB1(+) subband in InAs/GaSb QW. The spin orientations on the contour of CB1(−) subband are antiparallel to those of CB1(+) subband and are omitted in the figure for brevity. In the k-linear Rashba model, the spin orientations of an eigenstate is along $\hat{\boldsymbol{e}}_{\Sigma}=\hat{\boldsymbol{e}}_{\boldsymbol{k}_{\parallel}}\times\hat{\boldsymbol{e}}_{z}$, i.e., along the tangent direction of the circular energy contour in the QW plane.[42] However, this property no longer holds for InAs/AlSb/GaSb broken-gap QW. The spin orientations deviate strongly from the tangent direction $\hat{\boldsymbol{e}}_{\boldsymbol{k}_{\parallel}}\times\hat{\boldsymbol{e}}_{z}$, unless $\boldsymbol{k}_{\parallel}$ points along high-symmetry directions (such as $\langle 100\rangle$ and $\langle 110\rangle$) satisfying $\sin 4\varphi=0$. This comes from the hybridization between the spin-up and spin-down states, as discussed in the previous section. Therefore we can see the spin orientations on the contour $E=130$ meV deviate the most heavily because this contour is nearest to the maximum hybridization point, and when $\boldsymbol{k}_{\parallel}$ lies in the directions $\varphi=\pi/8, 3\pi/8$ ($\sin 4\varphi=\pm 1$), the maximum hybridization occurs. When we insert an AlSb barrier between InAs and GaSb layers, the hybridization is strongly reduced [Fig. 3(b)]. Thus the deviation of the spin orientation from the tangent direction is very small. The results of Fig. 3 imply that one can tune the spin orientations near the Fermi level by changing the thickness of AlSb barrier in the middle of InAs and GaSb layers.

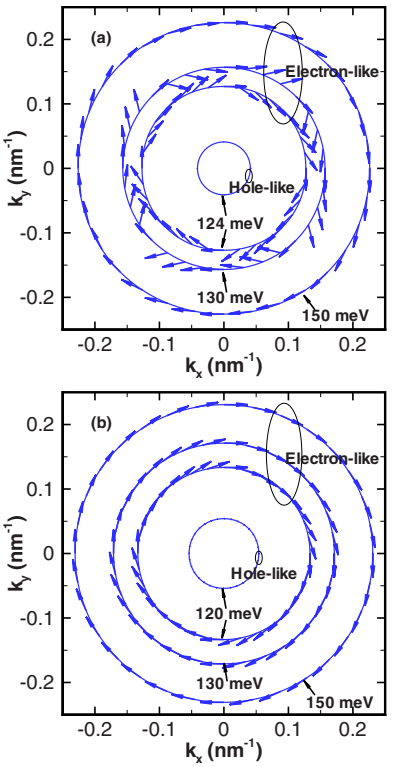

FIG. 3. (Color online) The spin orientations on the constant energy contours of CB1(+) subband of (a) a 10 nm InAs/10 nm GaSb QW and (b) a 10 nm InAs/2 nm AlSb/10 nm GaSb QW. Note the dominant components of the states of the insidest contours are $|HH(+)\rangle$ while that of the other contours are $|S(+)\rangle$.

Figure 4(a) exhibits the spin orientations for the states on different constant energy contours of VB1 subband in a InAs/GaSb QW. The energy contours of VB1 subband show a very complicated behavior and a strong anisotropy in the [100] and [110] directions due to the complicated band structures (see Fig. 2). From the figure, one can easily find a C_{4v} group symmetry, which comes from cubic symmetry of the crystal. For $E=113$ meV, we can find two pairs of contours. The states are electronlike for the inner but holelike for the outer pair. Due to the large spin splitting, the shape of energy contour for spin-up and spin-down state looks very different. If we insert an AlSb barrier between InAs and GaSb layers, the spin splitting between VB1(+) and VB1(−) is greatly reduced [see Fig. 4(b)].

In order to demonstrate the hybridization of the spin-up and spin-down states, we plot the components $|S(\pm)\rangle$, $|HH(\pm)\rangle$, and $|LH(\pm)\rangle$ of states in CB1($\pm$) subbands in Fig. 5. From this figure, one can see that the components $|HH(\pm)\rangle$ and $|S(\pm)\rangle$ varies significantly when increase $\boldsymbol{k}_{\parallel}$ over the anticrossing point $\boldsymbol{k}_{a}$.[9,10,32] Interestingly, at $\varphi=\pi/8$

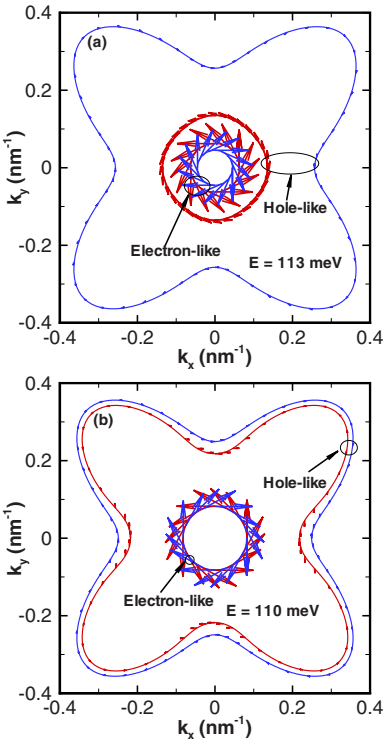

FIG. 4. (Color online) The spin orientations on the constant energy contours of VB1 subband of (a) a 10 nm InAs/10 nm GaSb QW and (b) a 10 nm InAs/2 nm AlSb/10 nm GaSb QW. The blue and red lines represent VB1(+) and VB1(−) branches, respectively.

direction, a strong hybridization between the spin-up state and spin-down state in the CB1 subbands occurs. This feature can be proven by the peak of spin-down component and the dip of spin-up component at $k_{\parallel}=0.145$ nm^{-1} in the CB1(+) subband. A similar behavior appears in the CB1(−)

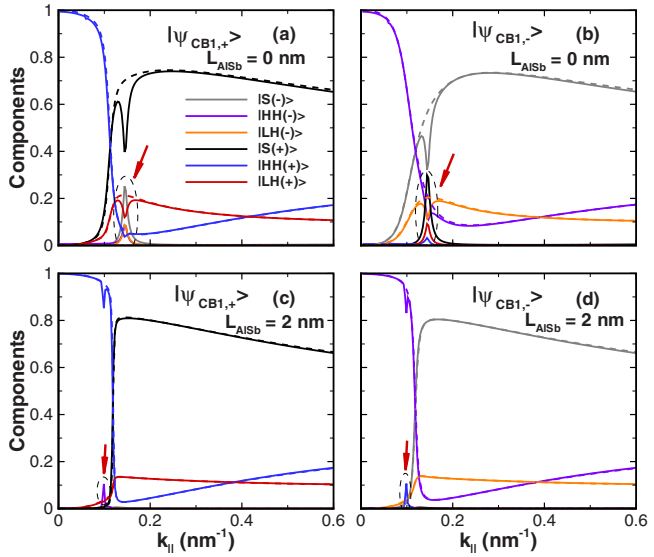

FIG. 5. (Color online) The components of states in CB1(±) subband as a function of $k_{\parallel}$ along $\varphi=\pi/8$ (solid line) and $\varphi=\pi/4$ ([110]) direction (dashed line) in [(a) and (b)] a 10 nm InAs/10 nm GaSb QW and [(c) and (d)] a 10 nm InAs/2 nm AlSb/10 nm GaSb QW. The red arrows indicate the maximum hybridization point.

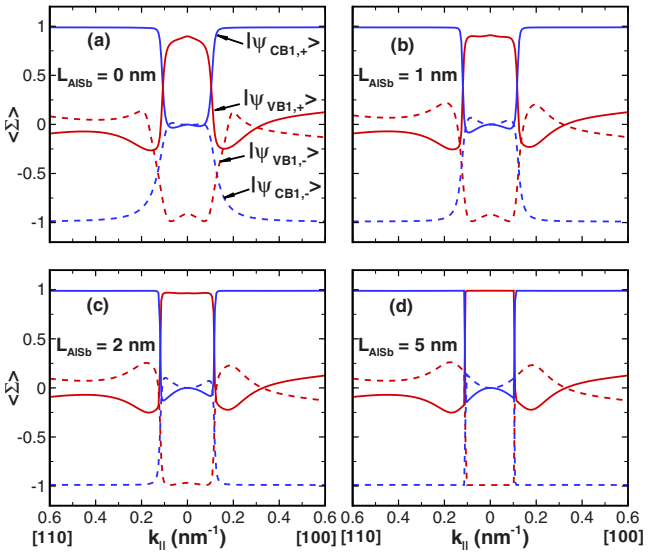

FIG. 6. (Color online) The projection of spin expectation values of $|\Psi_{\mathrm{CB1},\pm}\rangle$ and $|\Psi_{\mathrm{VB1},\pm}\rangle$ states along the orthogonal direction of $k_{\parallel}$ in InAs/AlSb/GaSb quantum well structures with different thicknesses of AlSb layers: (a) $L_{\mathrm{AlSb}}=0$, (b) $L_{\mathrm{AlSb}}=1$ nm, (c) $L_{\mathrm{AlSb}}=2$ nm, and (d) $L_{\mathrm{AlSb}}=5$ nm. The thickness of InAs and GaSb layers are fixed at 10 nm.

subband. For $k_{\parallel}$ along [110] ($\sin(4\varphi)=0$), there is no hybridization in the CB1 subbands and leading to pure spin-up and spin-down states. By inserting an AlSb barrier between InAs and GaSb layers, the holelike to electronlike transition of $|\Psi_{\mathrm{CB1},\pm}\rangle$ states become more emergent and the hybridization between spin-up or spin-down state is reduced.

As a result of the dominant component transition of the $|\Psi_{\mathrm{CB1},\pm}\rangle$ and $|\Psi_{\mathrm{VB1},\pm}\rangle$ states when $k_{\parallel}$ sweeps across the anticrossing point k_a, the spin expectation value magnitude $\langle\Sigma\rangle$ change correspondingly. In Fig. 6 we display the change in $\langle\Sigma\rangle$ for $|\Psi_{\mathrm{CB1},\pm}\rangle$ and $|\Psi_{\mathrm{VB1},\pm}\rangle$ states as a function of $k_{\parallel}$. $\langle\Sigma\rangle$ can be defined by projecting the vector $\langle\boldsymbol{\Sigma}\rangle$ onto $\hat{e}_{\Sigma}$, with $\hat{e}_{\Sigma}=\hat{e}_{k_{\parallel}}\times\hat{e}_z$ is the unit vector of the in-plane direction perpendicular to $k_{\parallel}$. A sudden change in $\langle\Sigma\rangle$ appears in Fig. 6 when $\mathbf{k}_{\parallel}$ sweeps across the anticrosssing point k_a so that the main characteristic of $|\Psi_{\mathrm{CB1},\pm}\rangle$ ($|\Psi_{\mathrm{VB1},\pm}\rangle$) states change from holelike (electronlike) to electronlike (holelike). In addition, we find sign reversals occur for $\langle\Sigma\rangle$ near the anticrossing points, which means the spin orientations do not maintain the same direction. This leads to the failure of recognizing the spin-up and spin-down branches simply by their spin orientations. Therefore we should classify the different spin states in a new set of basis functions as discussed in Sec. II B. Increasing the thickness of middle AlSb barrier, i.e., weakening of the interlayer coupling between InAs and GaSb layers, makes the smooth variation in $\langle\Sigma\rangle$ more and more sharp.

Besides the spin orientations in InAs/AlSb/GaSb QWs, it is interesting to discuss the zero-field spin splitting in these QWs because it can be directly measured from the experiments.[45] Therefore, we plot the RSS of CB1 and VB1 subbands as a function of the in-plane momentum in Fig. 7(a). From the figure, one can see a valley and sign reversal occurs in the RSS of CB1 subband, leading to the oscillating

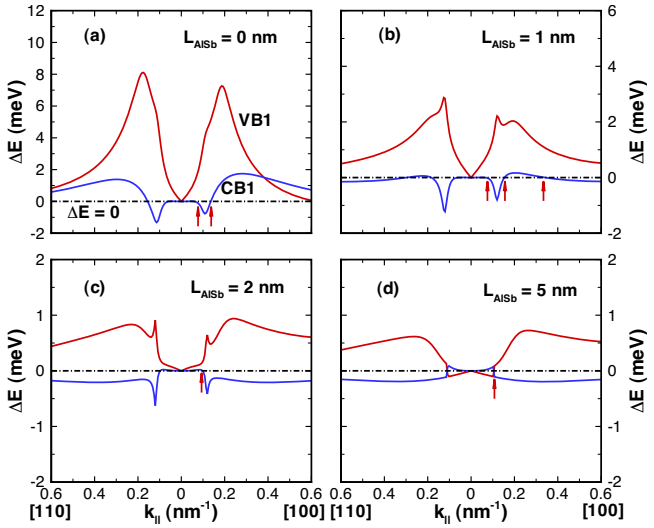

FIG. 7. (Color online) Rashba spin splitting of CB1 (blue line) and VB1 (red line) subbands in InAs/AlSb/GaSb quantum well structures with different thicknesses of AlSb layers: (a) $L_{\mathrm{AlSb}}=0$, (b) $L_{\mathrm{AlSb}}=1$ nm, (c) $L_{\mathrm{AlSb}}=2$ nm, and (d) $L_{\mathrm{AlSb}}=5$ nm. The thickness of InAs and GaSb layers are fixed at 10 nm. The red arrows mark the cross point between the curve of RSS and the dashdotted line $\Delta E=0$.

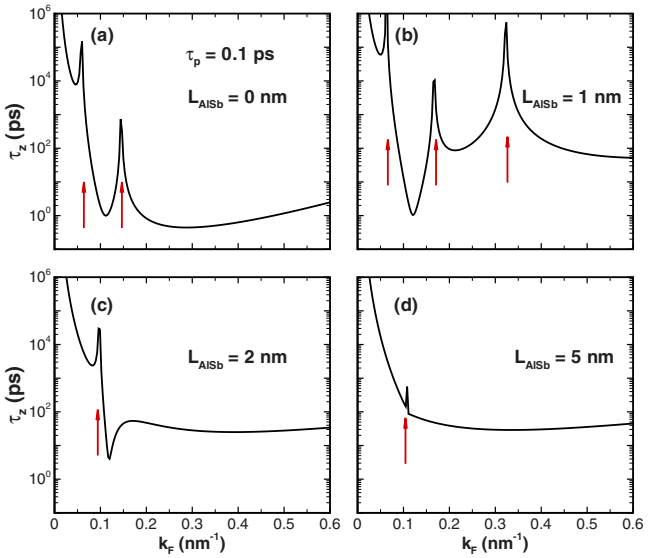

FIG. 8. (Color online) Dyakonov-Perel spin-relaxation time of CB1 subband as a function of Fermi wave vector k_F in InAs/AlSb/GaSb QWs with different thicknesses of AlSb layers: (a) $L_{\mathrm{AlSb}}=0$, (b) $L_{\mathrm{AlSb}}=1$ nm, (c) $L_{\mathrm{AlSb}}=2$ nm, and (d) $L_{\mathrm{AlSb}}=5$ nm. The red arrows mark the resonant peeks corresponding to the spin-degeneracy points.

behavior. This anomalous behavior arises from the difference between the anticrossing point between the CB1(+) and VB1(+) subbands and that between the CB1(−) and VB1(−) subbands. The decrease in RSS appearing at large $\boldsymbol{k}_{\parallel}$ is caused by the weakening of the conduction-valence-band coupling for carriers with large momentum, i.e., large kinetic energy or large effective bandgap.[46] In Fig. 7, we have marked the $\Delta E=0$ (spin-degeneracy) points with red arrows. By comparing to Fig. 5, we find these points actually lead to the maximum hybridized points in Fig. 5. The splitting of VB1 subband is much larger than that of CB1 subband. This reflects the fact that the spin-orbit coupling in valence band is much stronger than that of conduction band. An extremum appears in the RSS of VB1 subband near the anticrossing point. Figures 7(b)–7(d) shows the RSS of QWs with a AlSb barrier inserted between InAs and GaSb layers. When introducing an AlSb barrier into InAs/GaSb QW, the asymmetry at the left and right interfaces for InAs and GaSb layers is compensated, so the RSS of InAs/AlSb/GaSb QWs decreases greatly with increasing the thickness of AlSb layer. The valley in RSS of CB1 subband becomes sharper because the anticrossing behavior between the CB1 and VB1 subbands is heavily weakened as the AlSb barrier thickness increases. Interestingly, the anticrossing behavior seems like a crossing for the thick middle AlSb barrier, e.g., $L_{\mathrm{AlSb}}=5$ nm.

Since the spin splitting and spin states in InAs/GaSb and InAs/AlSb/GaSb broken-gap QWs are very different from that in conventional semiconductor QWs, the spin-related properties in these QWs should manifest a distinct feature as a consequence. As an example, the DP spin-relaxation time of CB1 subband in InAs/GaSb and InAs/AlSb/GaSb broken-gap QWs is calculated by taking axial approximation and based on the perturbation theory.[33] This theory demonstrates that the DP spin-relaxation rate $\tau_z^{-1}\propto\Omega^2\propto(\Delta E_{\mathrm{CB1}}^{ax})^2$, where Ω is the spin-obit coupling-induced in-plane effective magnetic field and proportional to the spin splitting $\Delta E_{\mathrm{CB1}}^{ax}$. The perturbation theory gives a clear physical picture about the DP spin relaxation that the DP spin-relaxation time would show resonant peaks when the spin splitting vanishes. As shown in Fig. 8, for a momentum relaxation time $\tau_p=0.1$ ps, we find the DP spin-relaxation time in these QWs varies from 1 to 10^5 ps with different k_F and the DP spin-relaxation time τ_z exhibits an obvious oscillating behavior. The resonant peaks (marked with the red arrows), actually corresponds to the $\Delta E=0$ in (spin-degeneracy) points Fig. 7. From panels (a)–(d), we can see the spin-relaxation time in InAs/AlSb/GaSb QWs is very sensitive to the thicknesses of middle AlSb layer. The oscillating and large-scale variation features of DP spin-relaxation time in InAs/GaSb/AlSb QWs are dramatically different from that in conventional semiconductor QWs. We suppose the unique features of spin-relaxation time InAs/GaSb/AlSb broken-gap QWs could provide us an interesting way to manipulate the evolution of electron spins.

In Fig. 9 we show the minigap as a function of the thickness of the middle AlSb barrier in InAs/AlSb/GaSb QWs. For fixed thickness of the InAs and GaSb layers of InAs/AlSb/GaSb QW, the minigap decrease rapidly with increasing thickness of the middle AlSb barrier, this feature was already demonstrated experimentally in Ref. 14, which shows that the minigap is about 1.75 meV for a InAs (15 nm)/GaSb (10 nm) QW and smaller than 0.3 meV for a InAs (15 nm)/AlSb (1.5 nm)/GaSb (15 nm) QW. The measured minigaps in Refs. 11–13 are 4, 7, and 2 meV, respectively. Based on our calculation, the minigap ranges from 0 to 4 meV, the magnitude of the minigap agree with the experiments. In general, we can see the minigaps reduce to zero rapidly as the thickness of the AlSb barrier increases. This is

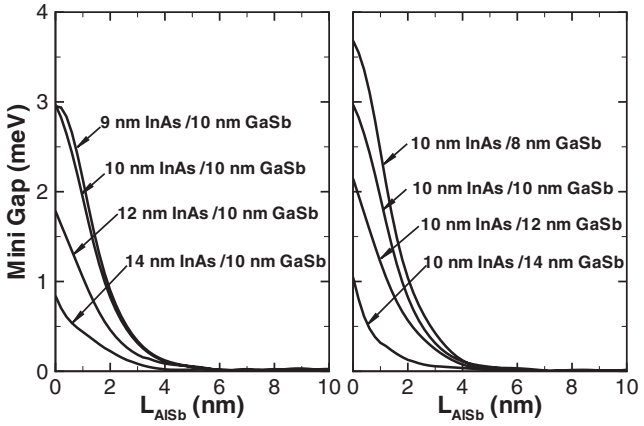

FIG. 9. Minigap as a function of the thickness of AlSb barrier in InAs/AlSb/GaSb QWs with (a) L_{GaSb} fixed at 10 nm and (b) L_{InAs} fixed at 10 nm.

because the tunneling between InAs conduction band and GaSb valence band is greatly suppressed by the AlSb barrier, so the electron-hole hybridization is restricted. In addition, if we fix AlSb barrier and increase the thickness of InAs layer or AlSb layer, the minigap decrease too. This is because the confining energy is reduced as the thickness of InAs layer or AlSb layers increases and the anticrossing point is then moved toward a higher $\boldsymbol{k}_{\parallel}$, which has less conduction-valence interband coupling strength and forms a smaller minigap. As the minigap and the hybridization degree change, the spin-related properties, including the spin orientations, spin splitting, and DP spin-relaxation time change consequently. Therefore we certainly find a method to tune the spin states in InAs/AlSb/GaSb QWs, which might be taken advantages in designing spintronic devices.

IV. CONCLUSION

We have investigated theoretically the spin orientation, spin splitting, and spin relaxation in InAs/AlSb/GaSb broken-gap QWs. We found the spin states in these broken-gap QWs are very different from that in conventional semiconductor QWs. The spin orientations deviate away from the tangent direction of the energy constant surface and the RSS of the anticrossed CB1 subband in InAs/AlSb/GaSb QWs exhibits a nonlinear and oscillating behavior. The deviation of spin orientation comes from the strong hybridization between different spin states, and the oscillating behavior of RSS is a result of the anticrossing of energy dispersions according. The distinct properties of RSS in InAs/AlSb/GaSb QWs lead to an oscillating behavior of DP spin-relaxation time obtained from the perturbation theory. By changing the thickness of AlSb barrier between the InAs and GaSb layers, the degree of hybridization can be tuned heavily, the mini-hybridization gap and spin orientations on the Fermi surface can be changed as a consequence. Our theoretical calculation is interesting both from the basic physics and potential application of the spintronic devices based on this novel broken-gap semiconductor QW system.

ACKNOWLEDGMENTS

This work was supported by the NSFC Grants No. 60525405 and No. 10874175, and bilateral program between Sweden and China.

APPENDIX: EIGHT-BAND SPIN MATRICES

Following the derivation of Winkler,[42] we can obtain the form of eight-band spin matrices vector in the basis set $(1h)$ by $\boldsymbol{\Sigma}' = \sigma \otimes \mathbb{L}_{orb}$, where $\sigma = (\sigma_x, \sigma_y, \sigma_z)$ is the vector of Pauli spin matrices and $\mathbb{L}_{orb}$ refers to the orbital part of the set basis function $(1h)$. The components $\Sigma'_x, \Sigma'_y, \Sigma'_z$ of $\boldsymbol{\Sigma}'$ can be written as

$$\Sigma'_x = \begin{bmatrix} 0 & 1 & 0 & 0 & 0 & 0 & 0 & 0 \\ 1 & 0 & 0 & 0 & 0 & 0 & 0 & 0 \\ 0 & 0 & 0 & \frac{i}{\sqrt{3}} & 0 & 0 & \frac{\sqrt{6}}{3} & 0 \\ 0 & 0 & -\frac{i}{\sqrt{3}} & 0 & \frac{2}{3}i & 0 & 0 & -\frac{\sqrt{2}}{3} \\ 0 & 0 & 0 & -\frac{2}{3}i & 0 & \frac{i}{\sqrt{3}} & \frac{\sqrt{2}}{3} & 0 \\ 0 & 0 & 0 & 0 & -\frac{i}{\sqrt{3}} & 0 & 0 & -\frac{\sqrt{6}}{3} \\ 0 & 0 & \frac{\sqrt{6}}{3} & 0 & \frac{\sqrt{2}}{3} & 0 & 0 & \frac{1}{3}i \\ 0 & 0 & 0 & -\frac{\sqrt{2}}{3} & 0 & -\frac{\sqrt{6}}{3} & -\frac{1}{3}i & 0 \end{bmatrix}, \tag{A1}$$

$$\Sigma'_y = \begin{bmatrix} 0 & -i & 0 & 0 & 0 & 0 & 0 & 0 \\ i & 0 & 0 & 0 & 0 & 0 & 0 & 0 \\ 0 & 0 & 0 & \frac{1}{\sqrt{3}} & 0 & 0 & -i\frac{\sqrt{6}}{3} & 0 \\ 0 & 0 & \frac{1}{\sqrt{3}} & 0 & \frac{2}{3} & 0 & 0 & i\frac{\sqrt{2}}{3} \\ 0 & 0 & 0 & \frac{2}{3} & 0 & \frac{1}{\sqrt{3}} & i\frac{\sqrt{2}}{3} & 0 \\ 0 & 0 & 0 & 0 & \frac{1}{\sqrt{3}} & 0 & 0 & -i\frac{\sqrt{6}}{3} \\ 0 & 0 & \frac{\sqrt{6}}{3}i & 0 & -\frac{\sqrt{2}}{3}i & 0 & 0 & \frac{1}{3} \\ 0 & 0 & 0 & -\frac{\sqrt{2}}{3}i & 0 & \frac{\sqrt{6}}{3}i & \frac{1}{3} & 0 \end{bmatrix}, \tag{A2}$$

$$\Sigma_z' = \begin{bmatrix} 1 & 0 & 0 & 0 & 0 & 0 & 0 & 0 \\ 0 & -1 & 0 & 0 & 0 & 0 & 0 & 0 \\ 0 & 0 & 1 & 0 & 0 & 0 & 0 & 0 \\ 0 & 0 & 0 & \frac{1}{3} & 0 & 0 & i\frac{2\sqrt{2}}{3} & 0 \\ 0 & 0 & 0 & 0 & -\frac{1}{3} & 0 & 0 & -i\frac{2\sqrt{2}}{3} \\ 0 & 0 & 0 & 0 & 0 & -1 & 0 & 0 \\ 0 & 0 & 0 & -\frac{2\sqrt{2}}{3}i & 0 & 0 & -\frac{1}{3} & 0 \\ 0 & 0 & 0 & 0 & \frac{2\sqrt{2}}{3}i & 0 & 0 & \frac{1}{3} \end{bmatrix}. \tag{A3}$$

Note that the set of basis functions we used are a little different from the basis used in Ref. 42, so the form of spin matrices [Eqs. (A1)–(A3)] are different from these in Ref. 42. Using Eq. (11), we can transform $\Sigma_x', \Sigma_y', \Sigma_z'$ into $\Sigma_x(\varphi), \Sigma_y(\varphi), \Sigma_z(\varphi)$, which are the components of eight-band spin matrices in the new basis set. $\Sigma_x(\varphi), \Sigma_y(\varphi), \Sigma_z(\varphi)$ can be written as

$$\Sigma_x(\varphi) = \begin{bmatrix} \mathcal{B}\sin\varphi & i\mathcal{C}\cos\varphi \\ -i\mathcal{C}^T\cos\varphi & \mathcal{D}\sin\varphi \end{bmatrix}, \tag{A4}$$

$$\Sigma_y(\varphi) = \begin{bmatrix} -\mathcal{B}\cos\varphi & i\mathcal{C}\sin\varphi \\ -i\mathcal{C}^T\sin\varphi & -\mathcal{D}\cos\varphi \end{bmatrix}, \tag{A5}$$

$$\Sigma_z(\varphi) = \begin{bmatrix} 0 & \mathcal{F} \\ \mathcal{F} & 0 \end{bmatrix}, \tag{A6}$$

where $\mathcal{B}$, $\mathcal{C}$, $\mathcal{D}$, and $\mathcal{F}$ are the 4×4 matrices,

$$\mathcal{B} = \begin{bmatrix} -1 & 0 & 0 & 0 \\ 0 & 0 & -\frac{1}{\sqrt{3}} & -\frac{\sqrt{6}}{3} \\ 0 & -\frac{1}{\sqrt{3}} & -\frac{2}{3} & \frac{\sqrt{2}}{3} \\ 0 & -\frac{\sqrt{6}}{3} & \frac{\sqrt{2}}{3} & -\frac{1}{3} \end{bmatrix},$$

$$\mathcal{C} = \begin{bmatrix} -1 & 0 & 0 & 0 \\ 0 & 0 & \frac{1}{\sqrt{3}} & \frac{\sqrt{6}}{3} \\ 0 & -\frac{1}{\sqrt{3}} & -\frac{2}{3} & \frac{\sqrt{2}}{3} \\ 0 & -\frac{\sqrt{6}}{3} & \frac{\sqrt{2}}{3} & -\frac{1}{3} \end{bmatrix},$$

$$\mathcal{D} = \begin{bmatrix} 1 & 0 & 0 & 0 \\ 0 & 0 & -\frac{1}{\sqrt{3}} & -\frac{\sqrt{6}}{3} \\ 0 & -\frac{1}{\sqrt{3}} & \frac{2}{3} & -\frac{\sqrt{2}}{3} \\ 0 & -\frac{\sqrt{6}}{3} & -\frac{\sqrt{2}}{3} & \frac{1}{3} \end{bmatrix}, \tag{A7}$$

$$\mathcal{F} = \begin{bmatrix} 1 & 0 & 0 & 0 \\ 0 & 1 & 0 & 0 \\ 0 & 0 & \frac{1}{3} & -\frac{2\sqrt{2}}{3} \\ 0 & 0 & -\frac{2\sqrt{2}}{3} & -\frac{1}{3} \end{bmatrix}.$$

For a pure spin-down state $|\Psi_{s,-}(k_\parallel)\rangle$, the expectation value of $\Sigma_x(\varphi), \Sigma_y(\varphi), \Sigma_z(\varphi)$ can be evaluated by

$$\langle\Sigma_x(\boldsymbol{k}_\parallel)\rangle_{s,-} = \langle\Psi_{s,-}(k_\parallel)|\Sigma_x(\varphi)|\Psi_{s,-}(k_\parallel)\rangle = \langle\mathcal{B}(k_\parallel)\rangle_{s,-}\sin\varphi, \tag{A8a}$$

$$\langle\Sigma_y(\boldsymbol{k}_\parallel)\rangle_{s,-} = \langle\Psi_{s,-}(k_\parallel)|\Sigma_y(\varphi)|\Psi_{s,-}(k_\parallel)\rangle = -\langle\mathcal{B}(k_\parallel)\rangle_{s,-}\cos\varphi, \tag{A8b}$$

$$\langle\Sigma_z(\boldsymbol{k}_\parallel)\rangle_{s,-} = \langle\Psi_{s,-}(k_\parallel)|\Sigma_z(\varphi)|\Psi_{s,-}(k_\parallel)\rangle = 0. \tag{A8c}$$

Similarly, for a pure spin-up state $|\Psi_{s,+}(k_\parallel)\rangle$, the expectation value of $\Sigma_x(\varphi), \Sigma_y(\varphi), \Sigma_z(\varphi)$ are

$$\langle\Sigma_x(\boldsymbol{k}_\parallel)\rangle_{s,+} = \langle\Psi_{s,+}(k_\parallel)|\Sigma_x(\varphi)|\Psi_{s,+}(k_\parallel)\rangle = \langle\mathcal{D}(k_\parallel)\rangle_{s,+}\sin\varphi, \tag{A9a}$$

$$\langle\Sigma_y(\boldsymbol{k}_\parallel)\rangle_{s,+} = \langle\Psi_{s,+}(k_\parallel)|\Sigma_y(\varphi)|\Psi_{s,+}(k_\parallel)\rangle = -\langle\mathcal{D}(k_\parallel)\rangle_{s,+}\cos\varphi, \tag{A9b}$$

$$\langle\Sigma_z(\boldsymbol{k}_\parallel)\rangle_{s,+} = \langle\Psi_{s,-}(k_\parallel)|\Sigma_x(\varphi)|\Psi_{s,-}(k_\parallel)\rangle = 0. \tag{A9c}$$

According to Eqs. (A8a) and (A9a), one can easily find $\boldsymbol{k}_\parallel\cdot\langle\boldsymbol{\Sigma}(\boldsymbol{k}_\parallel)\rangle_{s,\pm}=0$. Therefore, for pure spin-up states or spin-up states, the spin orientations are in the xy plane and strictly perpendicular to the in-plane wave vector.

*kchang@red.semi.ac.cn

[1] G. A. Sai-Halasz, R. Tsu, and L. Esaki, Appl. Phys. Lett. **30**, 651 (1977); G. A. Sai-Halasz, L. Esaki, and W. A. Harrison, Phys. Rev. B **18**, 2812 (1978).
[2] B. R. Bennett, R. Magno, J. B. Boos, W. Kruppa, and M. G. Ancona, Solid-State Electron. **49**, 1875 (2005).
[3] M. Altarelli, Phys. Rev. B **28**, 842 (1983); M. Altarelli, J. C. Maan, L. L. Chang, and L. Esaki, *ibid.* **35**, 9867 (1987).
[4] Y.-C. Chang and J. N. Schulman, Phys. Rev. B **31**, 2069 (1985).
[5] Y. Naveh and B. Laikhtman, Appl. Phys. Lett. **66**, 1980 (1995).
[6] J.-C. Chiang, S.-F. Tsay, Z. M. Chau, and I. Lo, Phys. Rev. Lett. **77**, 2053 (1996).
[7] S. de-Leon, L. D. Shvartsman, and B. Laikhtman, Phys. Rev. B **60**, 1861 (1999).
[8] R. Magri, L. W. Wang, A. Zunger, I. Vurgaftman, and J. R. Meyer, Phys. Rev. B **61**, 10235 (2000).
[9] E. Halvorsen, Y. Galperin, and K. A. Chao, Phys. Rev. B **61**, 16743 (2000).
[10] A. Zakharova, S. T. Yen, and K. A. Chao, Phys. Rev. B **64**, 235332 (2001); **66**, 085312 (2002).
[11] M. J. Yang, C. H. Yang, B. R. Bennett, and B. V. Shanabrook, Phys. Rev. Lett. **78**, 4613 (1997).
[12] M. Lakrimi, S. Khym, R. J. Nicholas, D. M. Symons, F. M. Peeters, N. J. Mason, and P. J. Walker, Phys. Rev. Lett. **79**, 3034 (1997).
[13] L. J. Cooper, N. K. Patel, V. Drouot, E. H. Linfield, D. A. Ritchie, and M. Pepper, Phys. Rev. B **57**, 11915 (1998).
[14] T. P. Marlow, L. J. Cooper, D. D. Arnone, N. K. Patel, D. M. Whittaker, E. H. Linfield, D. A. Ritchie, and M. Pepper, Phys. Rev. Lett. **82**, 2362 (1999).
[15] J. P. Cheng, J. Kono, B. D. McCombe, I. Lo, W. C. Mitchel, and C. E. Stutz, Phys. Rev. Lett. **74**, 450 (1995).
[16] Y. Naveh and B. Laikhtman, Phys. Rev. Lett. **77**, 900 (1996).
[17] D. Z. Y. Ting, D. A. Collins, E. T. Yu, D. H. Chow, and T. C. McGill, Appl. Phys. Lett. **57**, 1257 (1990).
[18] P. W. Ma and J. Wang, Phys. Rev. B **69**, 125308 (2004).
[19] J. Katz, Y. Zhang, and W. I. Wang, Appl. Phys. Lett. **62**, 609 (1993).
[20] R. Q. Yang, J. L. Bradshaw, J. D. Bruno, J. T. Pham, D. E. Wortman, and R. L. Tober, Appl. Phys. Lett. **81**, 397 (2002).
[21] T. Koga, J. Nitta, H. Takayanagi, and S. Datta, Phys. Rev. Lett. **88**, 126601 (2002).
[22] S. Datta and B. Das, Appl. Phys. Lett. **56**, 665 (1990).
[23] S. Hallstein, J. D. Berger, M. Hilpert, H. C. Schneider, W. W. Rühle, F. Jahnke, S. W. Koch, H. M. Gibbs, G. Khitrova, and M. Oestreich, Phys. Rev. B **56**, R7076 (1997).
[24] W. Yang, K. Chang, and S.-C. Zhang, Phys. Rev. Lett. **100**, 056602 (2008).
[25] C. Liu, T. L. Hughes, X.-L. Qi, K. Wang, and S.-C. Zhang, Phys. Rev. Lett. **100**, 236601 (2008).
[26] C. Petchsingh, R. J. Nicholas, K. Takashina, N. J. Mason, and J. Zeman, Phys. Rev. B **70**, 155306 (2004).
[27] K. Suzuki, K. Takashina, S. Miyashita, and Y. Hirayama, Phys. Rev. Lett. **93**, 016803 (2004).
[28] J. J. Quinn and J. J. Quinn, Surf. Sci. **361**, 930 (1996).
[29] M. I. Dyakonov and V. I. Perel, Sov. Phys. JETP **33**, 1053 (1971) [Zh. Eksp. Teor. Fiz. **60**, 1954 (1971)].
[30] B. A. Bernevig, J. Orenstein, and S.-C. Zhang, Phys. Rev. Lett. **97**, 236601 (2006).
[31] J. D. Koralek, C. P. Weber, J. Orenstein, B. A. Bernevig, S.-C. Zhang, S. Mack, and D. D. Awschalom, Nature (London) **458**, 610 (2009).
[32] J. Li, K. Chang, G. Q. Hai, and K. S. Chan, Appl. Phys. Lett. **92**, 152107 (2008).
[33] N. S. Averkiev and L. E. Golub, Phys. Rev. B **60**, 15582 (1999); N. S. Averkiev, L. E. Golub, and M. Willander, J. Phys.: Condens. Matter **14**, R271 (2002).
[34] Y. A. Bychkov and E. I. Rashba, J. Phys. C **17**, 6039 (1984).
[35] I. Lapushkin, A. Zakharova, S. T. Yen, and K. A. Chao, J. Phys.: Condens. Matter **16**, 4677 (2004).
[36] M. G. Burt, J. Phys.: Condens. Matter **4**, 6651 (1992); B. A. Foreman, Phys. Rev. B **56**, R12748 (1997); T. Darnhofer and U. Rossler, *ibid.* **47**, 16020 (1993).
[37] I. Vurgaftman, J. R. Meyer, and L. R. Ram-Mohan, J. Appl. Phys. **89**, 5815 (2001).
[38] W. Yang and K. Chang, Phys. Rev. B **72**, 233309 (2005).
[39] D. A. Broido and L. J. Sham, Phys. Rev. B **31**, 888 (1985).
[40] Calvin Yi-Ping Chao and S. L. Chuang, Phys. Rev. B **46**, 4110 (1992).
[41] The exact position of Fermi level in an undoped InAs/GaSb QW should locate inside the minigap (Refs. 3 and 28). The slight difference between our calculated E_F and the exact value comes from the summation of s in Eqs. (7) and (8) not running over all subbands in our calculation.
[42] R. Winkler, Phys. Rev. B **69**, 045317 (2004).
[43] R. Winkler, Phys. Rev. B **71**, 113307 (2005).
[44] R. Winkler, *Spin-orbit Coupling Effects in Two-dimensional Electron and Hole Systems* (Springer-Verlag, Berlin, 2003), Chap. 3, pp. 29–33.
[45] J. Luo, H. Munekata, F. F. Fang, and P. J. Stiles, Phys. Rev. B **38**, 10142 (1988).
[46] W. Yang and K. Chang, Phys. Rev. B **74**, 193314 (2006).